Gate-defined two-dimensional hole and electron systems in an undoped InSb quantum well

Zijin Lei [1,*] Erik Cheah [1] Filip Krizek [1,2,†] Rüdiger Schott [1] Thomas Bähler,[1] Peter Märki [1] Werner Wegscheider,[1,4] Mansour Shayegan [1,3] Thomas Ihn [1,4] and Klaus Ensslin [1,4]

[1]*Solid State Physics Laboratory, ETH Zurich, CH-8093 Zurich, Switzerland*
[2]*IBM Research Europe - Zurich, Säumerstrasse 4, 8803 Rüschlikon, Switzerland*
[3]*Department of Electrical and Computer Engineering, Princeton University, Princeton, New Jersey 08544, USA*
[4]*ETH Zurich Quantum Center, CH-8093 Zurich, Switzerland*

Quantum transport measurements are performed in gate-defined, high-quality, two-dimensional hole and electron systems in an undoped InSb quantum well. For both polarities, the carrier systems show tunable spin-orbit interaction as extracted from weak antilocalization measurements. The effective mass of InSb holes strongly increases with carrier density as determined from the temperature dependence of Shubnikov–de Haas oscillations. Coincidence measurements in a tilted magnetic field are performed to estimate the spin susceptibility of the InSb two-dimensional hole system. The *g* factor of the two-dimensional hole system decreases rapidly with increasing carrier density.

I. INTRODUCTION

Silicon, with both p-type and n-type transport characteristics, is the building block of today's complementary metal-oxide-semiconductor (CMOS) circuits. However, not every semiconductor exhibits high quality for both carrier types, and it is even more challenging to achieve ambipolar operation in a single device. Nowadays, in the widely used silicon CMOS technology, the integration of p- and n-type components is often achieved with sophisticated fabrication techniques. For example, ion implantation is adopted to reverse the polarity on the wafer locally [1–3]. In contrast with the established processes for silicon, many challenges still remain in devices based on III-V compounds, whose mobilities are in general much higher. The p- and n-type components in III-V devices mostly rely on different doping methods and materials, which have to be combined with specific metals for realizing Ohmic contacts [4,5]. So far, most approaches rely on complex bilayer system designs, where p- and n-type layers are grown subsequently along the growth direction. There, the two-dimensional electron and hole gases (2DEG and 2DHG) are produced either by different choice of dopants, different semiconductor materials, or by electrostatic gating using both a top-gate and a back gate [6–12]. Recently, incorporating both a high-quality 2DHG and a 2DEG into a single device became possible in two-dimensional (2D) materials, for example, in graphene, MoS$_2$, or black phosphorous [13–16], since in these materials one can contact carriers in both conduction bands and valence bands [17–21].

Narrow-gap III-V compounds such as InAs and InSb have also been proposed as systems that can potentially host both p- and n-type polarities [22,23]. InSb is known for the small effective mass of electrons and light holes in the bulk material, high carrier mobility at room temperature, strong spin-orbit interaction (SOI), and a large *g* factor in both the n- and p-type regimes [24–30]. These unique properties are interesting for potential applications such as high-frequency electronics [31], optoelectronics [32], and spintronics [33]. More recently, InSb, together with InAs, has attracted attention as a potential platform for topological quantum information processing [34–36]. Various low-dimensional n-type InSb systems have been studied, including quantum wells [37,38], nanowires [39,40], and other as-grown nanomaterials [41–43]. In previous work on n-type quantum wells we have shown that the parabolic band approximation agrees with experimental data [44–46]. On the contrary, for lower-dimensional, p-type InSb, similar to other p-type III-V compounds, the band structures are predicted to be more complicated than their n-type counterparts. In general, they strongly depend on the dimensions, shape of the potential well, global or local strain fields, SOI, and the carrier confinement [47–49]. Since the growth and processing methods for p-type devices are not as mature as for n-type, there is a lack of in-depth experimental studies of p-type InSb [50]. So far, quantum transport measurements have been reported for p-type InSb nanowires [51,52] and quantum wells [50]. Also, room-temperature experiments on p- and n-type InSb field-effect transistors were published [53]. However, limited by both the material quality and device design, the important properties of p-type InSb, such as scattering mechanisms, effective mass, *g* factor, and SOI, have not been precisely characterized.

In this work, we present quantum transport measurements on a gate-defined 2DHG and 2DEG in an ambipolar Hall bar device based on a single, undoped InSb quantum well.

---

*zilei@phys.ethz.ch
†Present address: Institute of Physics, Academy of Sciences of the Czech Republic, Cukrovarnicka 10, 162 00 Praha 6, Czech Republic.

Both the 2DHG and the 2DEG have relatively high mobility, even though the quantum well is close to the surface to allow for electrostatic top-gating. Shubnikov–de Haas (SdH) oscillations and the integer quantum Hall effect are observed for both carrier polarities. From the temperature dependence of SdH oscillations, we extract the effective mass of InSb holes and observe a large band nonparabolicity. Moreover, the strong and tunable SOI of both the 2DHG and the 2DEG is characterized by weak antilocalization (WAL) measurements. Finally, a coincidence measurement of the g factor in the 2DHG is performed, showing a strong dependence of the spin susceptibility on the carrier density.

II. SAMPLE PREPARATION

The InSb quantum well sample we discuss here is grown on a GaAs (100) substrate by molecular-beam epitaxy (MBE). The metamorphic buffer heterostructure, which is based on a previous publication by Lehner *et al.* [37], is used to filter the crystallographical defects related to the lattice mismatch. As shown in the high-angle-annular-dark-field (HAADF) scanning-transmission-electron-microscope (STEM) image of the InSb quantum well sample in Fig. 1(a), a 21.5-nm-thick InSb quantum well is sandwiched in-between $In_{0.9}Al_{0.1}Sb$ confinement barriers, with an 8.5-nm-thick top barrier and a 2-μm-thick bottom barrier. We note that there is no intentional doping during growth. Similar to Ref. [50], our InSb quantum well (QW) has a compressive strain of up to $\approx 0.53\%$, which is calculated from the lattice constants of $In_{0.9}Al_{0.1}Sb$ and InSb. The strain is also verified with the x-ray measurement (see Appendix).

After defining a standard $400 \times 200\,\mu m^2$ Hall bar using chemical etching, Ti/Au Ohmic contacts are evaporated. This combination of metals has been reported to provide Ohmic contacts for both p- and n-type InSb [51,52]. In the next step, the sample is coated with a 40-nm-thick aluminum oxide dielectric layer using atomic layer deposition (ALD) at 150 °C. Finally, a Ti/Au top-gate covering the Hall bar and overlapping the contacts is deposited by electron-beam evaporation, as illustrated in the inset of Fig. 1(b).

III. SHUBNIKOV–DE HAAS OSCILLATIONS AND INTEGER QUANTUM HALL EFFECTS

Transport measurements are performed using standard low-frequency lock-in techniques in a cryostat with a base temperature of 1.7 K. Figure 1(b) presents the two-terminal conductance $G_{1,4}$ between contacts 1 and 4 as a function of top-gate voltage V_{TG}. The conductance $G_{1,4}$ increases with increasing V_{TG} for positive voltages and with decreasing $V_{TG} < -2$ V. In between, the sample is insulating. This indicates that by sweeping V_{TG} from negative to positive, the polarity of the charge carriers changes from p-type to n-type, while in between, the Fermi level traverses the band gap. Comparing the up- and down-sweep of V_{TG} we find hysteresis, whose source still needs more study in future research. Therefore, we keep the sweep direction fixed for the following measurements. In the n-type regime, down-sweeps of V_{TG} are used, while up-sweeps are used in the p-type regime. Therefore, the data for both n- and p-type regimes are obtained during depleting the carriers.
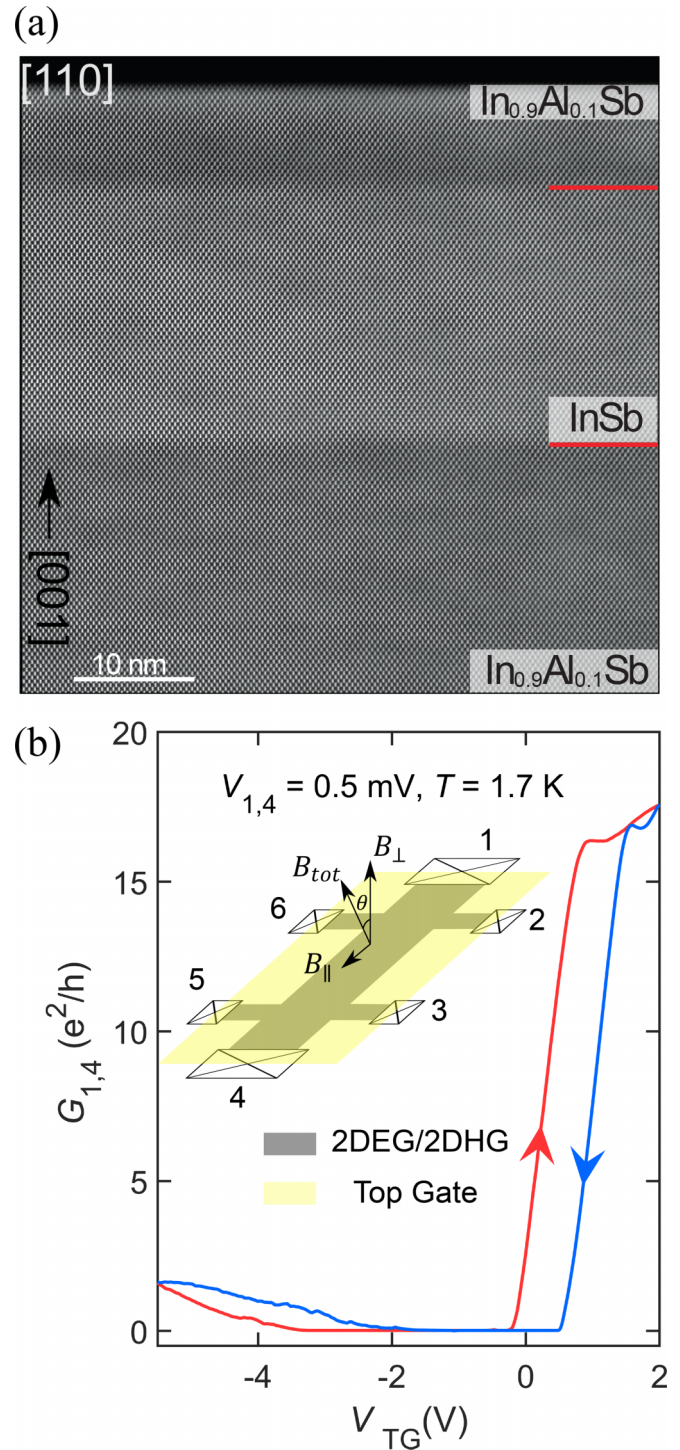
FIG. 1. (a) High-angle-annular-dark-field scanning transmission electron microscopic (HAADF STEM) image of the InSb quantum well and neighboring $In_{0.9}Al_{0.1}Sb$ barriers. There is no extended defects observed in the quantum well area. (b) Two-terminal conductance $G_{1,4}$ measured between contacts 1 and 4 vs top-gate voltage V_{TG}. A constant voltage of 0.5 mV is applied at 1.7 K. The blue and red traces show the down- and up-sweep, respectively. Inset shows a schematic diagram of the Hall bar sample and the definition of tilt angle θ. A global top-gate covers both the 2DEG or 2DHG and the contacts.
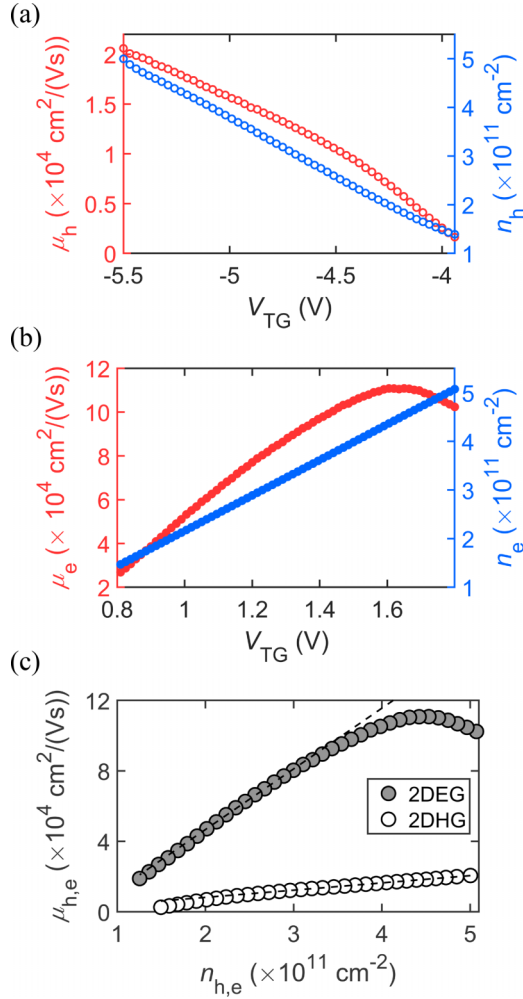
FIG. 2. (a), (b) Density and mobility vs V_{TG} measured in p- and n-type regimes, respectively. (c) The mobilities vs densities for both p- and n-types. The dashed lines are linear fits.

Now we measure the Hall bar sample with the standard method where a constant current is applied from contact 1 to contact 4. The longitudinal (between contact 2 and 3) and the transverse (between contact 3 and 5) resistivities, ρ_{xx} and ρ_{xy}, are measured. Figures 2(a) and 2(b) show the densities n_h of holes and n_e of electrons, determined from the classical Hall resistance (ρ_{xy}) at small magnetic fields, and the corresponding Drude mobilities μ_h and μ_e obtained from ρ_{xx} as a function of V_{TG}. Figure 2(c) summarizes the data into plots of density vs mobility for electrons and holes. The hole density n_h increases up to $5.0 \times 10^{11}\,\text{cm}^{-2}$ with decreasing V_{TG} and reaches the mobility $\mu_h = 21\,000\,\text{cm}^2/\text{V s}$. For comparison, also n_e increases up to $5 \times 10^{11}\,\text{cm}^{-2}$ with increasing V_{TG}, but the corresponding μ_e reaches its maximum of $1.1 \times 10^5\,\text{cm}^2/\text{V s}$ at $n_e = 4.5 \times 10^{11}\,\text{cm}^{-2}$ and starts to decrease beyond. The decreasing electron mobility at increasing density suggests that interface roughness scattering starts to dominate.

Figures 3(a) and 3(d) present ρ_{xx} and ρ_{xy} vs magnetic field B in the hole and the electron regimes, where $V_{TG} = -5.1\,\text{V}$ and $1.5\,\text{V}$, respectively. The densities of both holes and electrons are $4 \times 10^{11}\,\text{cm}^{-2}$. We find pronounced SdH oscillations

in ρ_{xx} and quantum Hall plateaus close to $\rho_{xy} = h/\nu e^2$, where ν is the integer filling factor, in both the p-type and n-type regimes. The 2DEG and the 2DHG show a Zeeman splitting in the SdH oscillations starting at and below very different filling factors ($\nu = 3$ for holes and $\nu = 9$ for electrons), indicating significant differences in effective mass and g factors between electrons and holes. Related measurements are discussed further below. Landau fan diagrams of ρ_{xx} and ρ_{xy} for both 2DHG and 2DEG are presented in Figures 3(b), 3(c) and 3(e), 3(f), respectively. The corresponding filling factors for 2DHG and 2DEG are labeled as ν_h and ν_e, respectively. Both regimes show the fan diagram of a single subband within the range of our measurements. Furthermore, for both 2DHG and 2DEG, there is no low-field, classical-positive magnetoresistance observed in ρ_{xx}. And, a positive magnetoresistance is a signature implying that more than one subband or layer is conductive [38,54,55]. These measurements, in both low-magnetic-field and high-magnetic-field regimes, demonstrate the high quality of both the single-channel 2DEG and 2DHG electrically induced in the same device. Both of them are single-band systems, without the second electronic subband populated and without a noticeable splitting of the heavy-hole band due to SOI [56]. We can quantitatively estimate Δn, the carrier density at which the second electronic subband starts to be populated. Using the infinite-high quantum well model, Δn is deduced to be $\approx 10 \times 10^{11}\,\text{cm}^{-2}$, which is much larger than n_e and n_h in this work.

IV. EFFECTIVE MASS AND BAND NON-PARABOLICITY OF TWO-DIMENSIONAL HOLES

In our previous work, we measured the effective mass of electrons in InSb quantum wells with the same thickness to be $\approx 0.016 m_e$ [38,44,46]. In the following, we present measurements of the effective mass of holes in the sample through the temperature dependence of the SdH oscillations at small magnetic fields. With the increase of the measurement temperature, the amplitude of the SdH oscillations will decrease until the oscillations vanish completely. The lower the effective mass, the higher the temperature at which the SdH oscillations can still be observed. The temperature dependence of the SdH oscillation is usually described by the Ando formula valid in the low-magnetic-field regime [57].

Figure 4(a) shows SdH oscillations for a hole density $n_h = 3.95 \times 10^{11}\,\text{cm}^{-2}$, measured at temperatures from 1.75 to 7 K. The oscillating part of the resistivity, $\Delta\rho_{xx}$, is obtained by subtracting the smooth background $\bar{\rho}_{xx}$ from the measured ρ_{xx}. We select the local maxima and minima in the traces of $\Delta\rho_{xx}$ vs B to extract the temperature dependence of the SdH oscillations and plot the quantity $\ln[\Delta\rho_{xx}T_0/(\bar{\rho}_{xx}T)]$ as a function of temperature in Fig. 4(b), where T_0 is the lowest temperature at which we measured the SdH oscillations. The effective mass $m^\star$ is then obtained by fitting to the function $-\ln[\sinh(2\pi^2 m^\star k_B T/\hbar e B)]$ with the effective mass being the fitting parameter. The deduced effective mass of holes is $m^\star = (0.046 \pm 0.003) m_e$, roughly constant within the magnetic-field range of the measurement [inset of Fig. 4(c)].

The quantum lifetime was extracted by fitting the data in Fig. 4(c) with the Dingle factor and using the effective mass determined above. At 1.75 K, we get a quantum
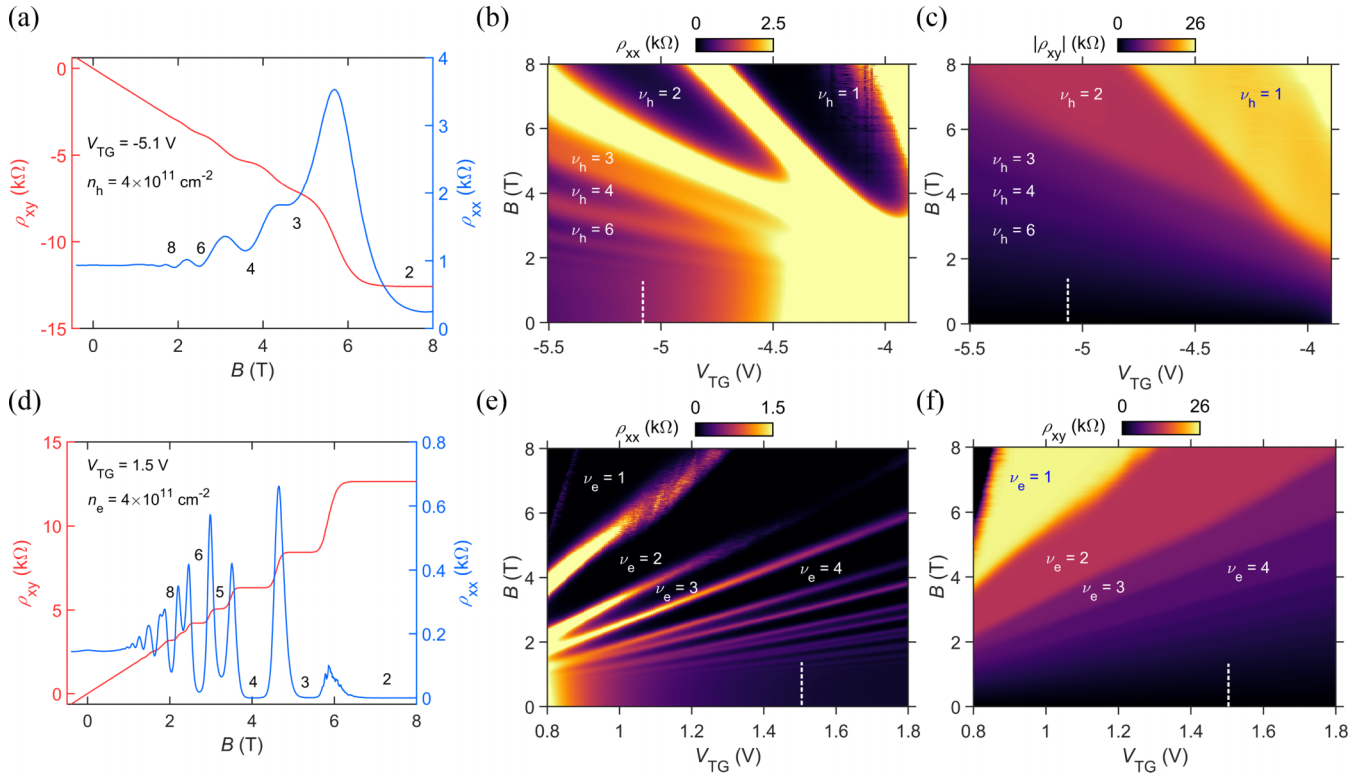
FIG. 3. (a) The SdH oscillations and integer quantum Hall effects of 2DHG. The filling factors are labeled in the figure. (b), (c) The Landau fan diagrams of 2DHG. Both ρ_{xx} and ρ_{xy} are presented. (d)–(f) Same as panels (a)–(c), but in the n-type regime. The filling factors for 2DHG and 2DEG are labeled as ν_h and ν_e, respectively. The white dashed lines correspond to the same carrier density 4×10^{11} cm^{-2} for both p- and n-types.

lifetime of $\tau_q = 110 \pm 10$ fs from the slope of the linear fit $\ln \Delta\rho_{xx}/(\Delta\bar{\rho}_{xx})f(B, T)$ vs $1/B$, where $f(B, T) = (2\pi^2 k_B T/\hbar\omega_c)/\sinh(2\pi^2 k_B T/\hbar\omega_c)$. The quantum lifetime τ_q is roughly a constant within the temperature range investigated. Considering the scattering time $\tau_{tr} = 0.435$ ps deduced from the Drude model at this carrier density, the Dingle ratio is $\tau_{tr}/\tau_q \approx 4$. With the same carrier density in the n-type regime, the Dingle ratio is about 20.8 in this device. The large difference of the Dingle ratio may imply a large difference in the scattering mechanism in 2DHG and 2DEG.

We repeat the measurement of the effective mass at different hole densities. In Fig. 4(d), $m^\star$ is plotted as a function of n_h. With the increase of n_h from 3.1 to 4.85×10^{11} cm^{-2}, the Fermi level shifts deeper into the valence band. At the same time, $m^\star$ increases from $0.03m_e$ to $0.057m_e$. This indicates a very large band nonparabolicity. Compared with the effective mass of holes in InSb bulk material, our results show a slightly larger value than for the light holes ($0.015m_e$) but a much smaller value than the effective mass of heavy holes ($\approx 0.43m_e$). This indicates that the band structure of p-type InSb may have similarities to p-type GaAs with the light-hole heave-hole degeneracy at the Γ point being lifted due to the confinement in the growth direction. Theory predicts that the in-plane effective mass of the heavy-hole band is smaller than that of the light-hole band (mass inversion) [56]. The effective mass depends strongly on density, which either implies that bands are strongly altered by self-consistent effects, or strongly nonparabolic bands, or both [48]. Compared with previous publications, our $m^\star$ are within the range of the

results obtained through theoretical calculations and cyclotron resonance measurements [49,50]. Nevertheless, the value of $m^\star$ for holes depends on many factors, including the shape and width of the quantum wells, the strain, the carrier densities, and possibly the SOI. Using the measured $m^\star$, we also obtain τ_q as a function of n_h [inset of Fig. 4(d)], showing an increase of τ_q with increasing carrier density, similar to mobility [Fig. 2(c)].

Using the values determined for $m^\star$, we qualitatively estimate the background impurity density n_{imp} in the heterostructure. Since $\mu_{h(e)}$ is proportional to $n_{h(e)}$ in a wide range, we may assume that scattering by ionized background impurities is the dominant scattering mechanism for both p- and n-type conduction [58]. Therefore, we estimate n_{imp} with

$$\frac{1}{\tau_{tr}} \approx \frac{n_{imp}m^\star}{2\pi \hbar^3 k_F^3}\left(\frac{e^2}{2\epsilon_0\epsilon_{InSb}}\right)^2 \int_0^{2k_F}\frac{q\,dq}{(q + q_{TF})^2\sqrt{1 - (q/2k_F)^2}},$$ (1)

where q_{TF} is the Thomas–Fermi wave vector, ϵ_{InSb} is the dielectric constant of InSb, and τ_{tr} is the mean scattering time due to background impurity scattering [59–61]. We calculate n_{imp} in the range where mobilities are proportional to carrier densities for 2DHG and 2DEG, respectively. n_{imp} is between 1.7×10^{17} and 3.8×10^{17} cm^{-3} when n_h is in a range of 3.0–4.7×10^{11} cm^{-2}. And when n_h is in a range of 1.2–3.0×10^{11} cm^{-2}, n_{imp} is between 1.3×10^{17} and 1.8×10^{17} cm^{-3}. This value is slightly higher than previous publications on InSb quantum wells [46,62] and InAs quantum wells [63].
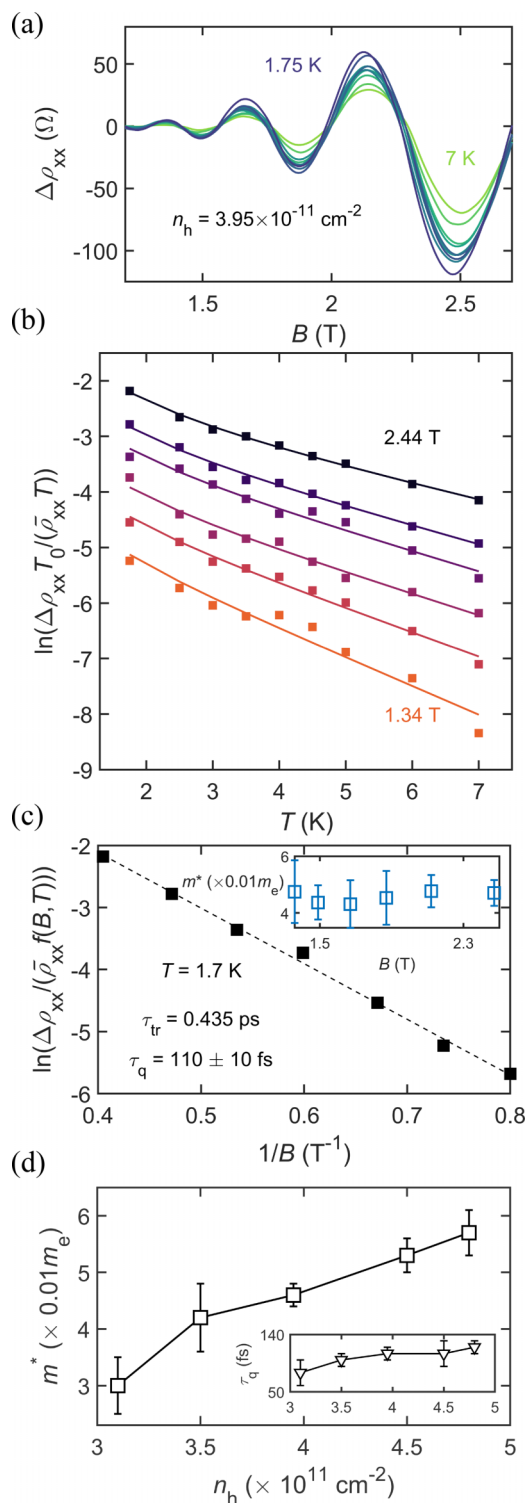
FIG. 4. Effective mass measurement for 2DHG. (a) Temperature dependence of SdH oscillations with $n_h = 3.95 \times 10^{11}$ cm^{-2}. (b) Dingle factor fitting at different B. The squares are data and the lines are fitted curves. (c) The fitting of the quantum lifetime at 1.75 K. Inset shows effective mass of holes vs B when $n_h = 3.95 \times 10^{11}$ cm^{-2}. (d) Effective mass as a function of carrier density. Error bars here are determined with the deviation of the fitting results. Inset shows the dependence of τ_q on n_h at 1.75 K.
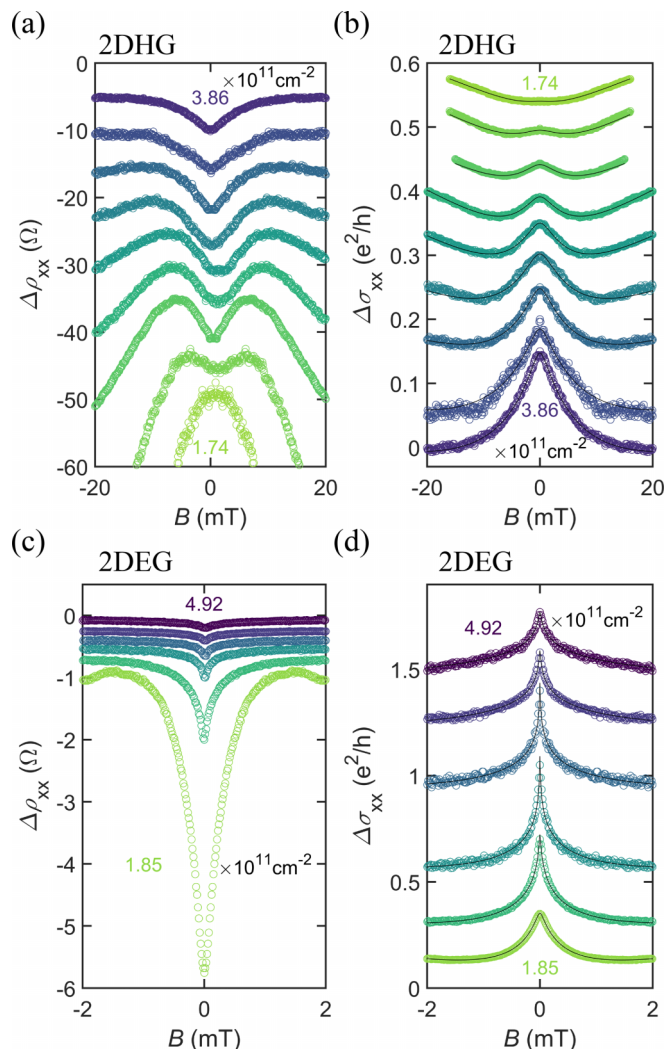
FIG. 5. Density dependence of WAL for both 2DHG and 2DEG. Panels (a) and (b) present $\Delta\rho_{xx}$ and $\Delta\sigma_{xx}$ vs B for 2DHG, respectively. Circles are the data while black curves are fits. (c), (d) Same as panels (a) and (b) but for the 2DEG. There are vertical offsets added in all the figures here for a clear presentation.

Then, it is worth comparing the mobilities of our 2DHG and 2DEG in the light of Eq. (1) considering the different effective masses of electrons and holes at $n_e = n_h = 3 \times 10^{11}$ cm^{-2}. If n_{imp} is the same for both 2DHG and 2DEG, this equation predicts $\mu_e/\mu_h \approx 2.4$. However, the measured mobility ratio is ≈ 6.2, showing that the mobility of 2DHG in our InSb quantum well is lower than this prediction. This is similar to the high-mobility GaAs 2D systems [60,64], and more investigation is needed to understand the scattering mechanism in InSb 2D systems quantitatively.

V. SPIN-ORBIT INTERACTION OF TWO-DIMENSIONAL HOLE GAS AND TWO-DIMENSIONAL ELECTRON GAS

Both the high-quality 2DHG and 2DEG in undoped InSb quantum wells display tunable SOI, which we characterize by WAL measurements. Figure 5 shows the WAL measurement at different carrier densities for the 2DHG and the 2DEG at 1.7 K, respectively. For the convenience of comparison, we

present $\Delta\rho_{xx}(B) = \rho_{xx}(B) - \rho_{xx}(0)$. To increase the signal-to-noise ratio, each trace presented represents the average of more than five consecutive measurements. In Fig. 5(a), with the increase of n_h from 1.74 to 3.86×10^{11} cm^{-2}, the local maximum of $\Delta\rho_{xx}$ at zero magnetic field develops into a minimum, which indicates the evolution from weak localization (WL) to WAL. Furthermore, in the WAL regime, $\Delta\rho_{xx}$ first increases and then decreases with the increase of the absolute value of B. At higher carrier densities, the turn-over magnetic field of $\Delta\rho_{xx}$ vs B moves to higher values. This implies an increase of the SOI with increasing n_h. For the 2DEG, we find WAL throughout the whole range of carrier densities which is from 1.85 to 4.92×10^{11} cm^{-2} [Fig. 5(c)]. Here we point out that whether the 2D system is in the WL or WAL regimes mainly depends on the ratio between l_{SO} and the mean-free-path l_e [57]. In our device, l_{SO}/l_e can be tuned over a larger range in the 2DHG than in the 2DEG. This is the reason why the evolution from the WL regime to the WAL regime is not observed in the 2DEG.

To understand this process in-depth, we extract the coherence length and the spin-orbit length using the Hikami-Larkin-Nagaoka (HLN) expression [65,66]. Similar methods were also adopted in publications where WAL effects were measured in doped InSb quantum wells [35], InSb nanosheets [67], and in our previous work [46]. As shown in Figs. 5(b) and 5(d), we convert the ρ_{xx} and ρ_{xy} to longitudinal conductivity σ_{xx} and subtract a classical polynomial background from the measurement in both p- and n-type regimes. The conductivity correction σ_{xx} of WALs reads

$$\Delta\sigma_{xx}(B) = \frac{e^2}{2\pi^2\hbar} \left\{ \Psi\left(\frac{1}{2} + \frac{H_\phi}{B} + \frac{H_{SO}}{B}\right) \right.$$
$$+ \frac{1}{2}\Psi\left(\frac{1}{2} + \frac{H_\phi}{B} + \frac{2H_{SO}}{B}\right)$$
$$- \frac{1}{2}\Psi\left(\frac{1}{2} + \frac{H_\phi}{B}\right) - \ln\left(\frac{H_\phi + H_{SO}}{B}\right)$$
$$\left. - \frac{1}{2}\ln\left(\frac{H_\phi + 2H_{SO}}{B}\right) + \frac{1}{2}\ln\frac{H_\phi}{B} \right\}. \quad (2)$$

Here, the two fitting parameters H_ϕ and H_{SO} are the phase-coherence field and the spin-orbit field, respectively, and Ψ is the digamma function. The two fitting parameters can be converted to phase-coherence length l_ϕ and spin-orbit length l_{SO} using $l_\phi = \sqrt{\hbar/4eH_\phi}$ and $l_{SO} = \sqrt{\hbar/4eH_{SO}}$. We first focus on the 2DHG. As shown in Fig. 6(a), the phase coherence length l_ϕ increases from 0.31 to 0.59 µm with the increase of n_h. The reduction of decoherence agrees with the increase of mobility. In contrast to l_ϕ, the spin-orbit length l_{SO} decreases from 0.37 to 0.18 µm, which indicates an increase of the SOI with higher n_h.

Like for other systems with strong SOI, we estimate the energy scales of the SOI with a parabolic band approximation [68,69]. Since we have determined the effective mass of the holes, Δ_{SO}, the energy splitting at the Fermi level due to SOI can be calculated according to $\Delta_{SO} = (2\hbar^2/\tau_{tr}\tau_{SO})^{1/2}$. The spin-orbit time τ_{SO} is calculated from $\tau_{SO} = \hbar/(4eDH_{SO})$. Here, $D = v_F^2\tau_{tr}/2$ is the diffusion constant in 2D with v_F being the Fermi velocity, which depends on $m^\star$. Then, we normalize Δ_{SO} to get the spin–orbit coefficient $\alpha_{SO} = \Delta_{SO}/2k_F$.
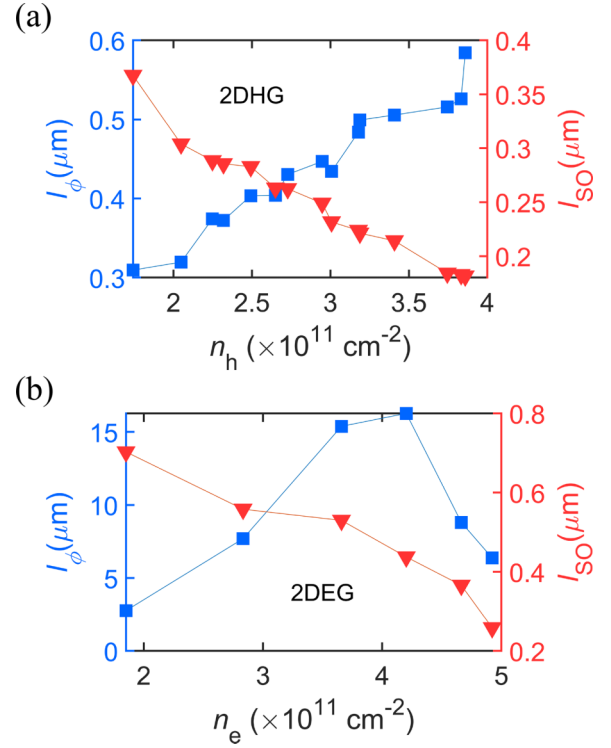
FIG. 6. l_{SO} and l_ϕ as a function of carrier density are presented for (a) 2DHG and (b) 2DEG.

The calculation shows that Δ_{SO} increases from 1.37 to 1.74 meV, while the spin-orbit coefficient α_{SO} is constant at ≈ 53 meVÅ. The constant α_{SO} is mainly due to the increasing mass. If we roughly estimate the Fermi energy using $E_F = \hbar^2 k_F^2/2m^\star$, the ratio Δ_{SO}/E_F increases from 5.2% to 8.2% in the range of n_h measured.

The results for the 2DEG are qualitatively similar to those for the 2DHG. Here, as shown in Fig. 6(b), l_{SO} decreases from 0.66 to 0.23 µm, which implies an increasing SOI with increasing n_e. For electrons, Δ_{SO} increases from 0.73 to 3.2 meV, and α_{SO} increases from 34 to 91 meVÅ. This value is approaching the results obtained recently in InAsSb quantum wells [70]. Interestingly, l_ϕ reaches a maximum of 16 µm and decreases with higher n_e. This is likely because of the mobility in the 2DEG, when the electron density n_e exceeds 4×10^{11} cm^{-2}.

VI. COINCIDENCE MEASUREMENTS OF TWO-DIMENSIONAL HOLE GAS

Finally, we present measurements of the spin susceptibility of the 2DHG using the coincidence method. This method has been introduced in previous publications [44,71]. The cyclotron energy is proportional to the perpendicular magnetic field $B_\perp$, while the Zeeman energy is proportional to the total magnetic field B_{tot}, if an isotropic g factor is assumed. The ratio between these two energies can be continuously changed by changing θ, the angle between the directions of sample normal and total magnetic field B_{tot} [inset of Fig. 1(b)]. Therefore, $B_\perp$, the projection of the magnetic field onto the sample

(a)

(b)
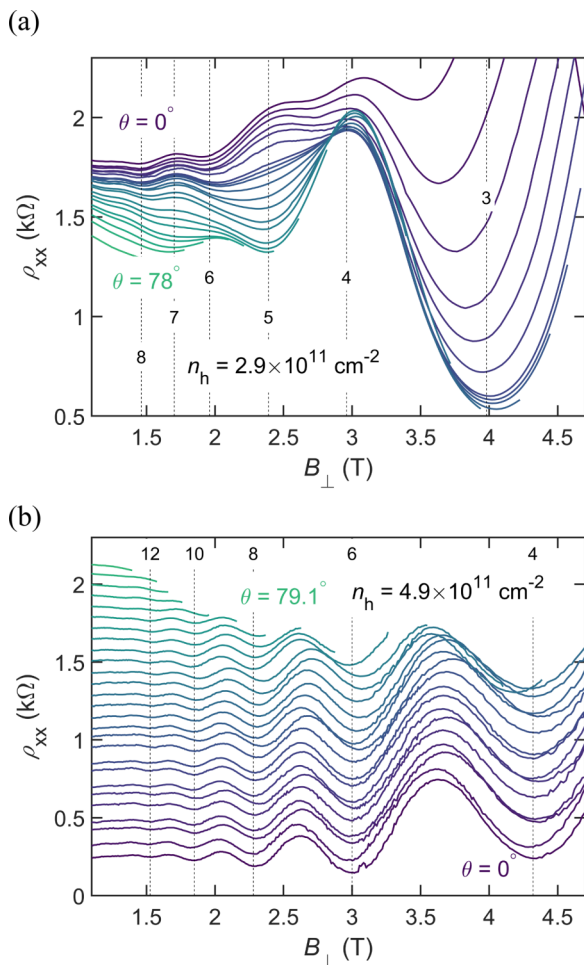
FIG. 7. (a), (b) The SdH oscillations measured for different tilt angles θ when $n_h = 2.9$ and 4.9×10^{11} cm^{-2}, respectively. For a better presentation, there is a constant vertical offset of 0.05 kΩ between each trace in panel (b) but no offset in panel (a). The filling factors are labeled with dashed lines.

normal, is $B_\perp = B_{tot} \cos \theta$. Here, we introduce the parameter:

$$r = \frac{|g^\star| \mu_B B_{tot}}{\hbar \omega_c} = \frac{|g^\star| \mu_B B_{tot}}{e \hbar B_\perp / m^\star} \quad (3)$$

to represent the ratio between Zeeman energy and cyclotron energy (μ_B is the Bohr magneton). Hence, we obtain $r \cos \theta = |g^\star| m^\star / 2m_e$. Whenever r takes integer values, SdH-minima in ρ_{xx} turn into maxima because the energy gap between the Landau levels neighboring in energy vanishes. The value of r can therefore be obtained by following the behavior of the local maxima and minima of ρ_{xx} for changing tilt angles θ. In general, for example in InAs and InSb 2DEGs, the value of ρ_{xx} at integer filling factors will change periodically between local minima and maxima, with increasing r [71,72]. Knowing r and θ, one can estimate the spin susceptibility to be $\chi = (|g^\star| m^\star)/(2 \pi \hbar^2)$.

Figure 7 shows ρ_{xx} as a function of $B_\perp$ with θ varying from 0 to $\approx 80°$ for densities $n_h = 2.9$ and 4.9×10^{11} cm^{-2}. The tilt angle θ is calibrated precisely (within 0.1°) using the Hall effect at small $B_\perp$. As shown in Fig. 7(a), despite being limited by the range of the magnetic field, we observe local

minima and maxima in $\rho_{xx}(B)$ to change as θ is increased. For instance, with increasing θ, the local ρ_{xx} maxima at $\nu_h = 5$ and 7 change to minima, while the pronounced minima at $\nu_h = 6$ and 4 change to maxima or vanish. This means that r is approaching 1 when we increase θ from 0 to 78°. As an estimation of the upper limit of the g factor, we assume $r \approx 1$ when $\theta \geqslant 78°$. This corresponds to a g factor $|g^\star| \leqslant 14$ for the measured $m^\star \approx 0.03 m_e$, if $m^\star$ is independent of B. This estimation of the g factor is in agreement with the value in bulk p-type InSb, which is ≈ 16 [24,56]. Here we also find that the local ρ_{xx} minima for $\nu_h = 4$ and 3 appear in smaller $B_\perp$ when $\theta = 0$. This could be because of the effect of attractive scattering centers in the quantum well in the low-density regime [73].

However, coincidence measurements at higher densities show different results. Figure 7(b) presents the coincidence measurement performed at $n_h = 4.9 \times 10^{11}$ cm^{-2}. Even when θ is increased to 79.1°, within the range of the magnetic field we can apply, there is no obvious dependence of ρ_{xx} on θ. Since p-type InSb is regarded to be a material with strong SOI and large g factor, it is unlikely that the g factor is so strongly reduced in the higher density regime that there is no observable change of ρ_{xx} up to $\theta = 79.1°$. Since we have observed that the SOI of the 2DHG increases significantly with increasing n_h, we hypothesize that the spin of the holes is locked with the orbits due to the larger SOI, implying a strongly anisotropic g factor. Similar results have been reported in other p-type quantum wells and also in 2D materials, such as MoS$_2$ [74,75]. Here we also note that the background of the SdH oscillations is independent of θ in the high-density regime. In contrast, the background shows a negative magneto-resistance with the increase of θ in the low-density regime. More studies are needed to understand this phenomenon.

VII. CONCLUSION

We have shown that both 2DHG and 2DEG can be induced by electrostatic gating in a single, shallow InSb heterostructure without any intentional doping. Thanks to the high quality of the sample, we are able to observe SdH oscillations and integer quantum Hall effects in both the p- and n-type regimes. In each regime, only a single electronic band is populated and contributes to transport. From the density dependence of the effective mass, we find that a large band nonparabolicity is present in the p-type regime. Furthermore, both 2DHG and 2DEG show tunable SOI. Finally, using coincidence measurements, we find that the spin susceptibility of InSb 2DHG strongly depends on the carrier density. Our work provides a better understanding of the detailed band structure and quantum properties of narrow-band gap III-V compounds, and paves the way for applications of InSb in high-mobility electronics and quantum information processing devices.
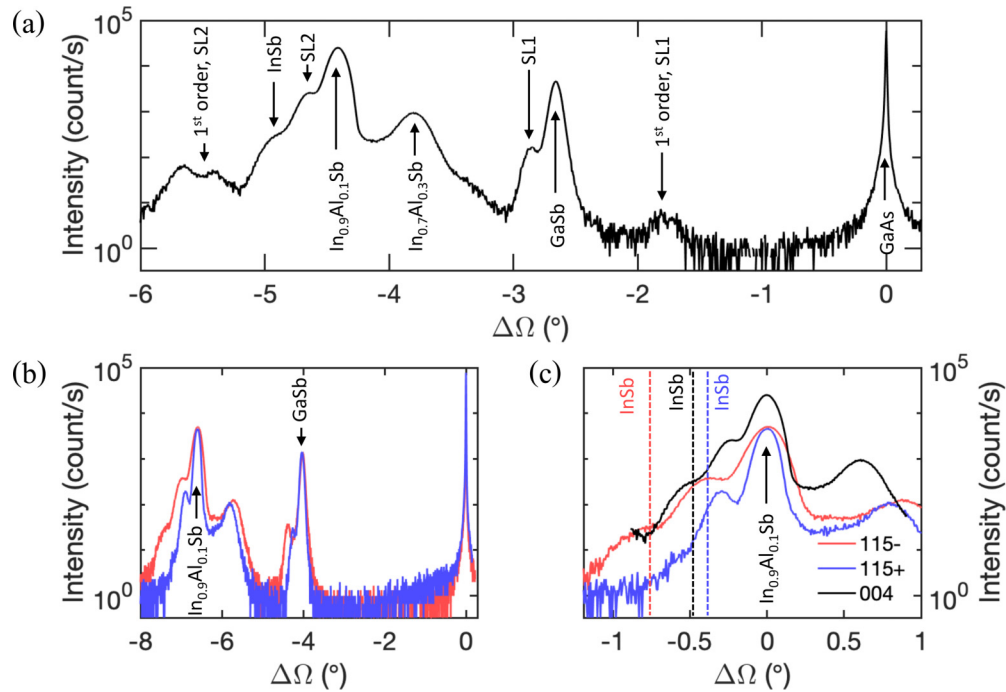
FIG. 8. (a) Symmetric (004) x-ray diffraction measurement. The x-ray rocking curve reveals the diffraction peaks of the GaAs substrate, the thick GaSb layer including the AlSb/GaSb superlattice (SL1), the $In_{1-x}Al_xSb$ layers including the InSb/$In_{1-x}Al_xSb$ superlattice (SL2), and the InSb QW. (b) Asymmetric (115−) and (115+) x-ray diffraction measurements. The rocking curves reveal that the respective peaks for GaSb and $In_{0.9}Al_{0.1}Sb$ lie on top of each other. From this, we conclude that the $In_{0.9}Al_{0.1}Sb$ and GaSb layer are relaxed compared with the GaAs substrate. (c) The dashed lines with red, blue, and black colors label the rough estimation of the relative peak positions from the InSb QW to the relaxed $In_{0.9}Al_{0.1}Sb$ layer. The position of the blue dashed line is set to fit the theoretical position when the QW is not relaxed. Nevertheless, the nonoverlaying peak positions can already indicate a strained InSb QW.

APPENDIX: X-RAY DIFFRACTION MEASUREMENT

Figure 8 shows x-ray rocking curves of the InSb quantum well (QW) heterostructure with the symmetric (004) direction together with the complementary directions (115−) and (115+). The measurements in the asymmetric diffraction geometry [Figs. 8(b) and 8(c)] show that the QW is strained because the peak positions of InSb with (115−) and (115+) directions do not overlap with each other. Due to the measurement limit, we can only determine a coarse position for the InSb QW layer [dashed lines in Fig. 8(c)]. As supported by the TEM image [Fig. 1(a) in the main text], which shows a defect-free QW region, the nonoverlaying peak positions of the InSb QW back up that the QW is grown pseudomorphically. Moreover, from Fig. 8(b), we can conclude that the $In_{0.9}Al_{0.1}Sb$ and GaSb layer are relaxed compared with the GaAs substrate. The $In_{0.9}Al_{0.1}Sb$ layer thereby serves as a virtual substrate for the InSb QW. Hence, a compressive strain up to 0.53% can be calculated from the lattice constants a of $In_{0.9}Al_{0.1}Sb$ ($a = 6.44501$ Å) and InSb ($a = 6.4794$ Å).

[1] J. Williams, Ion implantation of semiconductors, Mater. Sci. Eng., A **253**, 8 (1998).

[2] K. Küsters, H. Mühlhoff, and H. Cerva, Application of ion implantation in submicron CMOS processes, Nucl. Instrum. Methods Phys. Res., Sect. B **55**, 9 (1991).

[3] F. Mueller, G. Konstantaras, P. C. Spruijtenburg, W. G. van der Wiel, and F. A. Zwanenburg, Electron–hole confinement symmetry in silicon quantum dots, Nano Lett. **15**, 5336 (2015).

[4] H. L. Stormer, Z. Schlesinger, A. Chang, D. C. Tsui, A. C. Gossard, and W. Wiegmann, Energy Structure and Quantized Hall Effect of Two-Dimensional Holes, Phys. Rev. Lett. **51**, 126 (1983).

[5] T. Sajoto, Y. W. Suen, L. W. Engel, M. B. Santos, and M. Shayegan, Fractional quantum Hall effect in very-low-density GaAs/Al$_x$Ga$_{1-x}$As heterostructures, Phys. Rev. B **41**, 8449 (1990).

[6] D. Xiao, C.-X. Liu, N. Samarth, and L.-H. Hu, Anomalous Quantum Oscillations of Interacting Electron-Hole Gases in Inverted Type-II InAs/GaSb Quantum Wells, Phys. Rev. Lett. **122**, 186802 (2019).

[7] J. A. Seamons, D. R. Tibbetts, J. L. Reno, and M. P. Lilly, Undoped electron-hole bilayers in a GaAs/AlGaAs double quantum well, Appl. Phys. Lett. **90**, 052103 (2007).

[8] B. Kaestner, J. Wunderlich, D. G. Hasko, and D. Williams, Quasi-lateral 2DEG–2DHG junction in AlGaAs/GaAs, Microelectron. J. **34**, 423 (2003).

[9] A. Nakajima, Y. Sumida, M. H. Dhyani, H. Kawai, and E. S. Narayanan, High density two-dimensional hole gas induced by negative polarization at GaN/AlGaN heterointerface, Appl. Phys. Express **3**, 121004 (2010).

[10] M. Karalic, C. Mittag, T. Tschirky, W. Wegscheider, K. Ensslin, and T. Ihn, Lateral p-n Junction in an Inverted InAs/GaSb Double Quantum Well, Phys. Rev. Lett. **118**, 206801 (2017).

[11] W. Clarke, A. Micolich, A. Hamilton, M. Simmons, K. Muraki, and Y. Hirayama, Fabrication of induced two-dimensional hole systems on (311)A GaAs, J. Appl. Phys. **99**, 023707 (2006).

[12] R. Chu, Y. Cao, M. Chen, R. Li, and D. Zehnder, An experimental demonstration of GaN CMOS technology, IEEE Electron Device Lett. **37**, 269 (2016).

[13] A. K. Geim, Graphene: Status and prospects, Science **324**, 1530 (2009).

[14] A. H. Castro Neto, F. Guinea, N. M. R. Peres, K. S. Novoselov, and A. K. Geim, The electronic properties of graphene, Rev. Mod. Phys. **81**, 109 (2009).

[15] L. Li, Y. Yu, G. J. Ye, Q. Ge, X. Ou, H. Wu, D. Feng, X. H. Chen, and Y. Zhang, Black phosphorus field-effect transistors, Nat. Nanotechnol. **9**, 372 (2014).

[16] S. Chuang, C. Battaglia, A. Azcatl, S. McDonnell, J. S. Kang, X. Yin, M. Tosun, R. Kapadia, H. Fang, R. M. Wallace *et al.*, MoS$_2$ p-type transistors and diodes enabled by high work function MoO$_x$ contacts, Nano Lett. **14**, 1337 (2014).

[17] B. Zhan, C. Li, J. Yang, G. Jenkins, W. Huang, and X. Dong, Graphene field-effect transistor and its application for electronic sensing, Small **10**, 399 (2014).

[18] C. Dean, A. Young, L. Wang, I. Meric, G.-H. Lee, K. Watanabe, T. Taniguchi, K. Shepard, P. Kim, and J. Hone, Graphene based heterostructures, Solid State Commun. **152**, 1275 (2012).

[19] R. Wang, X.-G. Ren, Z. Yan, L.-J. Jiang, W. E. Sha, and G.-C. Shan, Graphene based functional devices: A short review, Front. Phys. **14**, 13603 (2019).

[20] Q. H. Wang, K. Kalantar-Zadeh, A. Kis, J. N. Coleman, and M. S. Strano, Electronics and optoelectronics of two-dimensional transition metal dichalcogenides, Nat. Nanotechnol. **7**, 699 (2012).

[21] C.-H. Lee, G.-H. Lee, A. M. van der Zande, W. Chen, Y. Li, M. Han, X. Cui, G. Arefe, C. Nuckolls, T. F. Heinz *et al.*, Atomically thin p–n junctions with van der Waals heterointerfaces, Nat. Nanotechnol. **9**, 676 (2014).

[22] T. Ashley, L. Buckle, S. Datta, M. Emeny, D. Hayes, K. Hilton, R. Jefferies, T. Martin, T. Phillips, D. Wallis *et al.*, Heterogeneous InSb quantum well transistors on silicon for ultra-high speed, low power logic applications, Electron. Lett. **43**, 777 (2007).

[23] G. Doornbos and M. Passlack, Benchmarking of III–V n-MOSFET maturity and feasibility for future CMOS, IEEE Electron Device Lett. **31**, 1110 (2010).

[24] I. Vurgaftman, J. R. Meyer, and L. R. Ram-Mohan, Band parameters for III–V compound semiconductors and their alloys, J. Appl. Phys. **89**, 5815 (2001).

[25] R. L. Kallaher, J. J. Heremans, N. Goel, S. J. Chung, and M. B. Santos, Spin-orbit interaction determined by antilocalization in an InSb quantum well, Phys. Rev. B **81**, 075303 (2010).

[26] G. A. Khodaparast, R. E. Doezema, S. J. Chung, K. J. Goldammer, and M. B. Santos, Spectroscopy of Rashba spin splitting in InSb quantum wells, Phys. Rev. B **70**, 155322 (2004).

[27] M. Leontiadou, K. Litvinenko, A. Gilbertson, C. Pidgeon, W. Branford, L. Cohen, M. Fearn, T. Ashley, M. Emeny, B. Murdin *et al.*, Experimental determination of the Rashba coefficient in InSb/InAlSb quantum wells at zero magnetic field and elevated temperatures, J. Phys.: Condens. Matter **23**, 035801 (2011).

[28] A. M. Gilbertson, W. R. Branford, M. Fearn, L. Buckle, P. D. Buckle, T. Ashley, and L. F. Cohen, Zero-field spin splitting and spin-dependent broadening in high-mobility InSb/In$_{1-x}$Al$_x$Sb asymmetric quantum well heterostructures, Phys. Rev. B **79**, 235333 (2009).

[29] J. Orr, P. D. Buckle, M. Fearn, C. Storey, L. Buckle, and T. Ashley, A surface-gated InSb quantum well single electron transistor, New J. Phys. **9**, 261 (2007).

[30] O. Madelung, U. Roessler, and M. Schulz, *Landolt-Bernstein-Group III Condensed Matter, 41D* (Springer, Berlin, 2000).

[31] T. Ashley, A. B. Dean, C. T. Elliott, G. J. Pryce, A. D. Johnson, and H. Willis, Uncooled high-speed InSb field-effect transistors, Appl. Phys. Lett. **66**, 481 (1995).

[32] H. Chen, J. Heremans, J. Peters, A. Govorov, N. Goel, S. Chung, and M. Santos, Spin-polarized reflection in a two-dimensional electron system, Appl. Phys. Lett. **86**, 032113 (2005).

[33] I. Žutić, J. Fabian, and S. D. Sarma, Spintronics: Fundamentals and applications, Rev. Mod. Phys. **76**, 323 (2004).

[34] Y. Oreg, G. Refael, and F. von Oppen, Helical Liquids and Majorana Bound States in Quantum Wires, Phys. Rev. Lett. **105**, 177002 (2010).

[35] C. T. Ke, C. M. Moehle, F. K. de Vries, C. Thomas, S. Metti, C. R. Guinn, R. Kallaher, M. Lodari, G. Scappucci, T. Wang *et al.*, Ballistic superconductivity and tunable π-junctions in InSb quantum wells, Nat. Commun. **10**, 3764 (2019).

[36] M. Deng, S. Vaitiekėnas, E. B. Hansen, J. Danon, M. Leijnse, K. Flensberg, J. Nygård, P. Krogstrup, and C. M. Marcus, Majorana bound state in a coupled quantum-dot hybrid-nanowire system, Science **354**, 1557 (2016).

[37] C. A. Lehner, T. Tschirky, T. Ihn, W. Dietsche, J. Keller, S. Fält, and W. Wegscheider, Limiting scattering processes in high-mobility InSb quantum wells grown on GaSb buffer systems, Phys. Rev. Mater. **2**, 054601 (2018).

[38] Z. Lei, C. A. Lehner, E. Cheah, M. Karalic, C. Mittag, L. Alt, J. Scharnetzky, W. Wegscheider, T. Ihn, and K. Ensslin, Quantum transport in high-quality shallow InSb quantum wells, Appl. Phys. Lett. **115**, 012101 (2019).

[39] H. A. Nilsson, P. Caroff, C. Thelander, M. Larsson, J. B. Wagner, L.-E. Wernersson, L. Samuelson, and H. Q. Xu, Giant, level-dependent *g* factors in InSb nanowire quantum dots, Nano Lett. **9**, 3151 (2009).

[40] H. A. Nilsson, O. Karlström, M. Larsson, P. Caroff, J. N. Pedersen, L. Samuelson, A. Wacker, L.-E. Wernersson, and H. Q. Xu, Correlation-Induced Conductance Suppression at Level Degeneracy in a Quantum Dot, Phys. Rev. Lett. **104**, 186804 (2010).

[41] M. de la Mata, R. Leturcq, S. R. Plissard, C. Rolland, C. Magén, J. Arbiol, and P. Caroff, Twin-induced InSb nanosails: A convenient high mobility quantum system, Nano Lett. **16**, 825 (2016).

[42] N. Kang, D. Fan, J. Zhi, D. Pan, S. Li, C. Wang, J. Guo, J. Zhao, and H. Xu, Two-dimensional quantum transport in free-standing InSb nanosheets, Nano Lett. **19**, 561 (2019).

[43] J. Xue, Y. Chen, D. Pan, J.-Y. Wang, J. Zhao, S. Huang, and H. Xu, Gate defined quantum dot realized in a single crystalline InSb nanosheet, Appl. Phys. Lett. **114**, 023108 (2019).

[44] Z. Lei, C. A. Lehner, K. Rubi, E. Cheah, M. Karalic, C. Mittag, L. Alt, J. Scharnetzky, P. Märki, U. Zeitler, W. Wegscheider, T. Ihn, and K. Ensslin, Electronic *g* factor and magnetotransport in InSb quantum wells, Phys. Rev. Res. **2**, 033213 (2020).

[45] Z. Lei, C. A. Lehner, E. Cheah, C. Mittag, M. Karalic, W. Wegscheider, K. Ensslin, and T. Ihn, Gate-defined quantum point contact in an InSb two-dimensional electron gas, Phys. Rev. Res. **3**, 023042 (2021).

[46] Z. Lei, E. Cheah, K. Rubi, M. E. Bal, C. Adam, R. Schott, U. Zeitler, W. Wegscheider, T. Ihn, and K. Ensslin, High-quality two-dimensional electron gas in undoped InSb quantum wells, Phys. Rev. Res. **4**, 013039 (2022).

[47] J. P. Eisenstein, H. L. Störmer, V. Narayanamurti, A. C. Gossard, and W. Wiegmann, Effect of Inversion Symmetry on the Band Structure of Semiconductor Heterostructures, Phys. Rev. Lett. **53**, 2579 (1984).

[48] E. Marcellina, A. R. Hamilton, R. Winkler, and D. Culcer, Spin-orbit interactions in inversion-asymmetric two-dimensional hole systems: A variational analysis, Phys. Rev. B **95**, 075305 (2017).

[49] C. E. Pryor and M.-E. Pistol, Band-edge diagrams for strained III-V semiconductor quantum wells, wires, and dots, Phys. Rev. B **72**, 205311 (2005).

[50] C. K. Gaspe, M. Edirisooriya, T. D. Mishima, P. A. R. D. Jayathilaka, R. E. Doezema, S. Q. Murphy, M. B. Santos, L. C. Tung, and Y.-J. Wang, Effect of strain and confinement on the effective mass of holes in InSb quantum wells, J. Vac. Sci. Technol., B: Nanotechnol. Microelectron.: Mater., Process., Meas., Phenom. **29**, 03C110 (2011).

[51] H. A. Nilsson, M. T. Deng, P. Caroff, C. Thelander, L. Samuelson, L.-E. Wernersson, and H. Q. Xu, InSb nanowire field-effect transistors and quantum-dot devices, IEEE J. Sel. Top. Quantum Electron. **17**, 907 (2011).

[52] V. S. Pribiag, S. Nadj-Perge, S. M. Frolov, J. W. V. D. Berg, I. V. Weperen, S. R. Plissard, E. P. Bakkers, and L. P. Kouwenhoven, Electrical control of single hole spins in nanowire quantum dots, Nat. Nanotechnol. **8**, 170 (2013).

[53] M. Radosavljevic, T. Ashley, A. Andreev, S. Coomber, G. Dewey, M. Emeny, M. Fearn, D. Hayes, K. Hilton, M. Hudait *et al.*, High-performance 40 nm gate length InSb p-channel compressively strained quantum well field effect transistors for low-power ($V_{CC} = 0.5$ V) logic applications, in *2008 IEEE International Electron Devices Meeting, San Francisco, CA, USA* (IEEE, 2008), pp. 1–4.

[54] D. K. Efetov, P. Maher, S. Glinskis, and P. Kim, Multiband transport in bilayer graphene at high carrier densities, Phys. Rev. B **84**, 161412(R) (2011).

[55] E. Zaremba, Transverse magnetoresistance in quantum wells with multiple subband occupancy, Phys. Rev. B **45**, 14143 (1992).

[56] R. Winkler, *Spin-Orbit Coupling Effects in Two-Dimensional Electron and Hole Systems* (Springer, Berlin, 2003).

[57] T. Ihn, *Semiconductor Nanostructures: Quantum States and Electronic Transport* (Oxford University Press, Oxford, UK, 2010).

[58] V. Umansky, R. De-Picciotto, and M. Heiblum, Extremely high-mobility two dimensional electron gas: Evaluation of scattering mechanisms, Appl. Phys. Lett. **71**, 683 (1997).

[59] J. H. Davies, *The Physics of Low-Dimensional Semiconductors, An Introduction* (Cambridge University Press, Cambridge, UK, 1993).

[60] Y. J. Chung, C. Wang, S. K. Singh, A. Gupta, K. W. Baldwin, K. W. West, M. Shayegan, L. N. Pfeiffer, and R. Winkler, Record-quality GaAs two-dimensional hole systems, Phys. Rev. Mater. **6**, 034005 (2022).

[61] Y. J. Chung, A. Gupta, K. W. Baldwin, K. W. West, M. Shayegan, and L. N. Pfeiffer, Understanding limits to mobility in ultrahigh-mobility gaas two-dimensional electron systems: 100 million cm^2/V s and beyond, Phys. Rev. B **106**, 075134 (2022).

[62] W. Yi, A. A. Kiselev, J. Thorp, R. Noah, B.-M. Nguyen, S. Bui, R. D. Rajavel, T. Hussain, M. F. Gyure, P. Kratz *et al.*, Gate-tunable high mobility remote-doped InSb/In$_{1-x}$Al$_x$Sb quantum well heterostructures, Appl. Phys. Lett. **106**, 142103 (2015).

[63] T. Tschirky, S. Mueller, C. A. Lehner, S. Fält, T. Ihn, K. Ensslin, and W. Wegscheider, Scattering mechanisms of highest-mobility InAs/Al$_x$Ga$_{1-x}$Sb quantum wells, Phys. Rev. B **95**, 115304 (2017).

[64] S. Ahn and S. Das Sarma, Density-dependent two-dimensional optimal mobility in ultra-high-quality semiconductor quantum wells, Phys. Rev. Mater. **6**, 014603 (2022).

[65] S. Hikami, A. I. Larkin, and Y. Nagaoka, Spin-orbit interaction and magnetoresistance in the two dimensional random system, Prog. Theor. Phys. **63**, 707 (1980).

[66] S. V. Iordanskii, Y. B. Lyanda-Geller, and G. E. Pikus, Weak localization in quantum wells with spin-orbit interaction, Pis'ma Zh. Eksp. Teor. Fiz. **60**, 199 (1994).

[67] Y. Chen, S. Huang, D. Pan, J. Xue, L. Zhang, J. Zhao, and H. Xu, Strong and tunable spin–orbit interaction in a single crystalline InSb nanosheet, npj 2D Mater. Appl. **5**, 3 (2021).

[68] V. Senz, T. Heinzel, T. Ihn, K. Ensslin, G. Dehlinger, D. Grützmacher, and U. Gennser, Coexistence of weak localization and a metallic phase in Si/SiGe quantum wells, Phys. Rev. B **61**, R5082 (2000).

[69] B. Grbić, R. Leturcq, T. Ihn, K. Ensslin, D. Reuter, and A. D. Wieck, Strong spin-orbit interactions and weak antilocalization in carbon-doped *p*-type GaAs/Al$_x$Ga$_{1-x}$As heterostructures, Phys. Rev. B **77**, 125312 (2008).

[70] S. Metti, C. Thomas, D. Xiao, and M. J. Manfra, Spin-orbit coupling and electron scattering in high-quality InSb$_{1-x}$As$_x$ quantum wells, Phys. Rev. B **106**, 165304 (2022).

[71] S. Brosig, K. Ensslin, A. G. Jansen, C. Nguyen, B. Brar, M. Thomas, and H. Kroemer, InAs-AlSb quantum wells in tilted magnetic fields, Phys. Rev. B **61**, 13045 (2000).

[72] H. Schumacher, A. Nauen, U. Zeitler, R. Haug, P. Weitz, A. Jansen, and F. Schäffler, Anomalous coincidences between valley split Landau levels in a Si/SiGe heterostructure, Phys. B (Amsterdam, Neth.) **256-258**, 260 (1998).

[73] R. J. Haug, R. R. Gerhardts, K. v. Klitzing, and K. Ploog, Effect of Repulsive and Attractive Scattering Centers on the

Magnetotransport Properties of a Two-Dimensional Electron Gas, Phys. Rev. Lett. **59**, 1349 (1987).

[74] Q. Shi, M. A. Zudov, C. Morrison, and M. Myronov, Strong transport anisotropy in Ge/SiGe quantum wells in tilted magnetic fields, Phys. Rev. B **91**, 201301(R) (2015).

[75] R. Pisoni, Y. Lee, H. Overweg, M. Eich, P. Simonet, K. Watanabe, T. Taniguchi, R. Gorbachev, T. Ihn, and K. Ensslin, Gate-defined one-dimensional channel and broken symmetry states in MoS_2 van der Waals heterostructures, Nano Lett. **17**, 5008 (2017).